Delft University of Technology

Influence of the manufacturing process on the stress state of curved glulam beams

Yu, Taoyi; Khaloian, Ani; van de Kuilen, Jan Willem

Important note
To cite this publication, please use the final published version (if applicable).
Please check the document version above.

Influence of the manufacturing process on the stress state of curved glulam beams

Taoyi Yu [a,*] , Ani Khaloian [a], Jan-Willem van de Kuilen [a, b]

[a] *Professorship of Wood Technology, Department of Materials Engineering, School of Engineering and Design, Technical University of Munich, Munich, Germany*
[b] *Biobased Structures and Materials, Faculty of Civil Engineering and Geosciences, Delft University of Technology, Delft, The Netherlands*

HIGHLIGHTS

- Thorough analysis of formation mechanism of different residual stress components in curved glulam.
- Identification of the transverse residual stresses that are not covered by the current design standard.
- Parametric study on the geometric and material parameters that influence the residual stresses.
- Random growth-ring between boards cause additional stress concentrations.

ARTICLE INFO

ABSTRACT

This study examines the spring-back effect and residual stresses in curved glued-laminated timber (glulam) beams during the manufacturing process. In addition to curving along the longitudinal axis (X), a cup-deformation develops in the transverse direction (Z) due to the Poisson's effect. This deformation, combined with the glue-hardening process and the release of pressure, leads to the development of residual stresses in all three axial directions, as well as shear stresses within individual boards and at their interfaces.

Besides the well-known factors such as longitudinal elasticity, board thickness, and inner radius, the study reveals that the number of layers (n) and Poisson's ratio (v_{LT}) significantly influence the magnitude of residual stresses. However, aside from longitudinal stresses, the impact of n and v_{LT}, as well as other residual stresses, have been scarcely studied and are not adequately addressed in current design standards.

A Monte–Carlo analysis of the growth-ring effect is conducted, taking the pith location of different board layers as the input random variable. Strong influences can be identified on the residual stresses in both radial and tangential directions, with intensified maximum values and more scattered distribution inside the cross-section. The time- and moisture-dependent relaxation analysis using the rheological wood model shows a significant influence of the temperature and relative humidity.

1. Introduction

Glued-laminated timber (glulam) has been gaining popularity in modern construction due to its advantages including high strength-weight ratio, sustainability, aesthetic value, as well as adaptability to various shapes, such as curved or pitched glulams. It is commonly used in arches, roofs, and bridges with different spans and curvatures for maximizing interior space, reducing the height of exterior walls at supports, and aligning the beam depth with the bending moment diagram [1].

However, compared to the straight beams, the stress state inside the curved beams becomes more complex. Because of the curvature, the internal fibers in curved beams are shorter than the external ones, causing a shift of the neutral axis, as illustrated in Fig. 1(c) and consequently leading to non-linear distributions of longitudinal and perpendicular to grain stresses (Fig. 1(d)) irrespective of the material used, and the development of a stress perpendicular to the grain (Fig. 1(e)).

It is important to note that the tensile strength perpendicular to the grain is notably low [2]. Consequently, numerous failures under tension
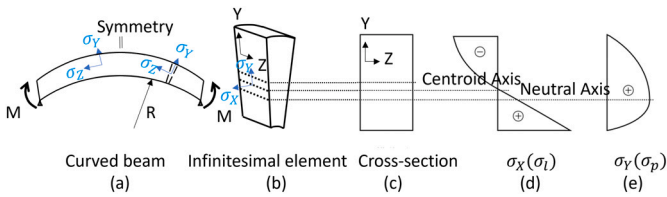
Fig. 1. Elastic theory solutions of bending stresses in a curved beam.

perpendicular to the grain are documented in the summary work by Dietsch et al. [3], Franke et al. [4], as well as Frese and Blaß [5], and various reinforcement strategies targeting these stresses are detailed in studies by Blaß et al. [6], Jönsson [7], and Fueyo et al. [8].

Besides the standard manufacturing procedures which include finger jointing, gluing, and finishing, to achieve the desired curvature, additional specifications are required for the press, adhesives, and custom molds. Since Otto Hetzer's patent in 1906 for the bent wooden components [9], the demand for complex curved glulam beams has increased, driving advancements in manufacturing technology [10]. As a result, significant residual stresses can develop during the manufacturing process. As demonstrated in [11], an innovative bamboo–timber composite beam utilizes these residual stresses as a form of prestressing to enhance structural performance. Despite this novel application, residual stresses are more commonly regarded as detrimental, often reducing the load-carrying capacity of the final curved glulam products. In Eurocode 5 [12], the influence of manufacturing residual stresses in the longitudinal direction is included, such that the longitudinal stress (σ_L) is required to be less than the product of the strength (f_L) and a safety coefficient k_r:

$$k_r = \begin{cases} 1 & \text{for } \frac{R_1}{t} \geq 240 \\ 0.76 + 0.001\frac{R_1}{t} & \text{for } \frac{R_1}{t} < 240 \end{cases} \quad (1)$$

where R_1 is the inner radius of the beam, and t is the thickness of a single lamella.

However, as indicated by Fig. 1, the stresses developed during manufacturing can be more complicated than just those in the longitudinal direction, and varying growth-ring patterns between different board layers as well as the time- and moisture-dependent effects can also influence the stress state [13,14]. Moreover, as the strength in the transverse direction is relatively small [2] and often serves as the major design criterion

for curved beams, even a small magnitude of transverse stress, when combined with the transverse service stress, can lead to earlier damage to the beam [15].

Fig. 2 shows the major stages of a curved glulam beam, including *Single Boards*, *Manufacturing*, *In Storage*, and *In Service*.

The *Manufacturing* process takes approximately 24 hours, depending on the requirements of the specific glue type. The exact hardening time, however, is usually not specified in the product information. According to the work of Maas et al. [16], where a bilayer flexion reporter system combined with inverse calibration method is designed, the hardening time is found to vary from 0.26 hours to 1.52 hours, depending on different wood species and glue types. In their method, hardening is assumed to be an instantaneous process, such that the glue changes at this time-point from a frictionless liquid to a solid that restricts any relative movement between the two board surfaces.

The *In Storage* state includes the stages of storage, transportation to the building site, and assembly on site. Ideally, the whole process occurs under constant environmental conditions; in reality, temperature (T) and relative humidity (RH) vary, leading to fluctuations in the moisture content of the beam.

The *In Service* state describes the time after the beam is assembled, when mechanical loads are applied. Additionally, depending on the service class, the beam may experience varying levels of moisture fluctuations.

As wood is a time- and moisture-sensitive material [17], it is important to identify the time and possible moisture fluctuations during the stages which can lead to shrinkage stress along with mechano-sorptive relaxation. Fig. 3 shows the major sources of the moisture fluctuations which are the moisture interchange between boards, moisture absorbed/desorbed from glues, and the moisture fluctuation due to the temperature and relative humidity changes of the environment. The study on the quantification of the moisture amount as well as the corresponding stress can be found in [16,18–21].

Additionally, the anisotropy and inhomogeneity of wood can result in stress concentration and consequently strength reduction, which have been analyzed in multiple works through stochastic models [22–25]. Glulam, as an engineered product composed of multiple wood layers, presents an additional source of inhomogeneity—the growth ring variation between layers [20]. Such influence was identified experimentally in [21] and has been analyzed through Monte–Carlo simulations in [26,27]. However, most of the aforementioned stochastic studies focus on bending or moisture-induced stress, leaving a gap in the analysis of stress concentrations that may occur during the manufacturing process.
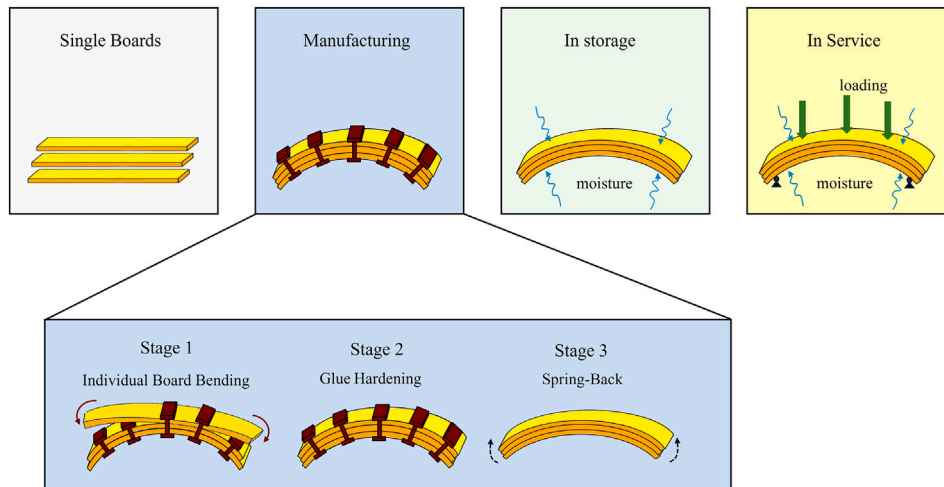

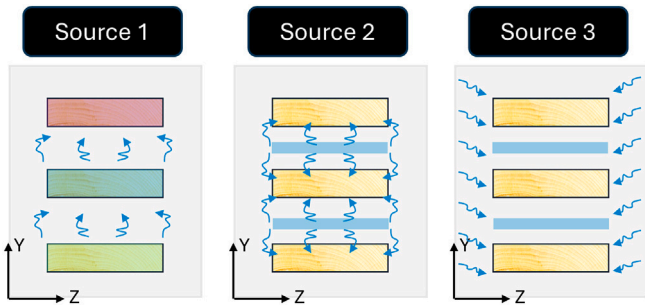**Fig. 2.** Sketch of the major states of a curved glulam.

Fig. 3. Source of moisture.

In this work, the following issues regarding the residual stresses will be addressed:

1. analysis of the formation mechanisms of all components of the residual stress,
2. parameter study of the geometric and material parameters,
3. evaluation of influence of the layups of board layers with random growth-ring patterns,
4. evaluation of the viscoelastic and mechano-sorptive relaxation of the residual stress.

2. Materials and method

2.1. Finite element model

As shown in Fig. 2, The *Manufacturing* state can be further divided into three main stages:

- *Real Stage 1*: Individual boards are bent to the desired curvature after applying the glue on the surfaces. In practice, the curvature is usually controlled by a clamping system. For larger beams, to reduce the required force and for more precise control, boards are bent in sequence by releasing and refixing the clamps.
- *Real Stage 2*: The boards are left under the clamping for a certain length of time until the glue is solidified. Typically, additional pressure is maintained through the clamping system to ensure full contact between boards for the proper solidification of glue.

- *Real Stage 3*: After sufficient time, the clamps are released. The curvature of the boards is maintained by the glues. Typically, due to the removal of the external bending moment, a spring-back occurs.

As shown in Fig. 4, for stress analysis, the stages of interest are, however, different from the real ones. If the time- and moisture-dependent behavior is neglected for the short period during *Real Stage 2*, the stress remains unchanged. However, due to the Poisson's effect, in the transverse direction, the cross-section can also undergo complex deformation and therefore exhibit significant residual stress. To understand the formation of the stress, two-time points during *Real Stage 1* can be considered important, which are then identified as *Model Stages 1* and *2* as shown in Fig. 4.

- *(Model) Stage 1*:
  Condition:
  All the board layers are bent to the desired curvature, but the clamps are not fully tightened, allowing the cross-section to deform freely.
  Anticipated Deformation:
  In the longitudinal direction, the fibers are elongated of each individual board in the upper part and shortened in the lower part.
  Additionally. Due to Poisson's effect, in the transverse Z direction, the upper part will shrink and the lower part will expand, resulting in cup deformation with a curvature ($R'_{in,i}$). Moreover, unlike in the longitudinal direction where the outer radius $R_{out,i} = R_{in,i-1}$, the curvature between the bottom surface ($R'_{out,i}$) and the top surface ($R'_{out,i-1}$) does not match, as highlighted in red circles.
  Anticipated Stress:
  For each single board, longitudinal and radial stress are developed corresponding to the curvature $R_{in,i-1}$, following the distribution shown in Fig. 1. No addition stress is formed in the Z or Y direction as deformation is allowed freely.
- *(Model) Stage 2*:
  Condition:
  The clamps are tightened, leaving no void between different board layers.
  Anticipated Deformation:
  The top and bottom surfaces of each board are flattened.
  Anticipated Stress:
  The stress in the longitudinal direction remains unchanged. However, in the transverse Z direction, Compared to the previous
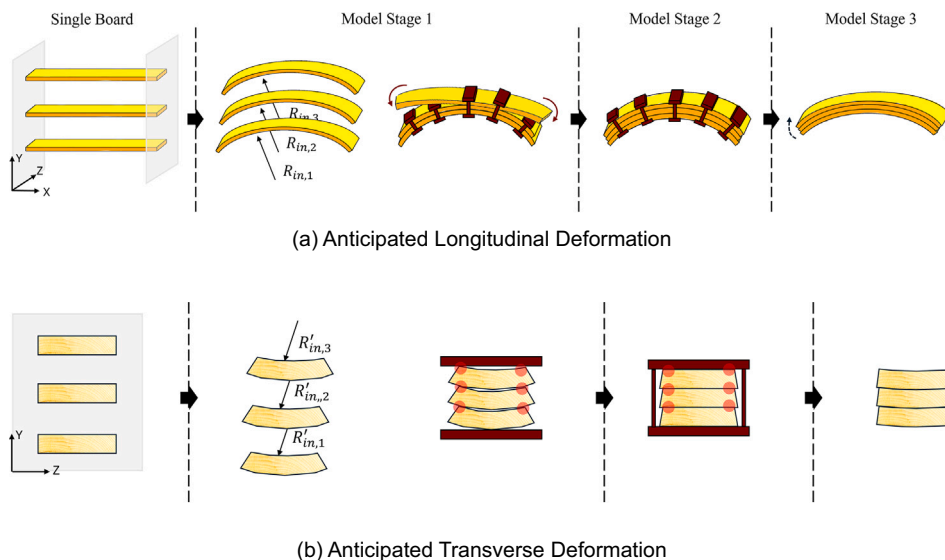

(a) Anticipated Longitudinal Deformation

(b) Anticipated Transverse Deformation

Fig. 4. Sketch of the three *Model Stages* during manufacturing process.
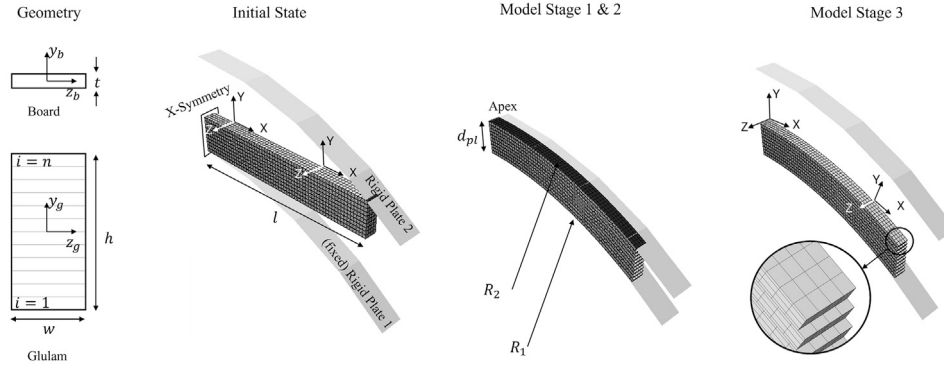
Fig. 5. Model overview.

stage, the upper part of each board gets elongated and the lower part gets shortened, resulting in tension on the top and compression on the bottom.

Additionally, due to the mismatched curvature ($R'_{out,i}$ and $R'_{out,i-1}$) from the previous stage, stress concentration can occur at the two sides of the beam, highlighted in red circles in Fig. 4(b).

- *(Model) Stage 3*:

  Condition:

  All clamps are removed.

  Anticipated Deformation:

  In the longitudinal direction, the curvature of the entire beam gets bigger, which is commonly called the spring-back effect. In the transverse direction, due to the removal of the clamps, the cup deformation can be recovered to a certain extent, especially for the outermost boards. Yet, the extent of the recovery is reduced for the boards in the middle layers.

  Anticipated Stress:

  The spring-back effect can alter the stress formed in *Stage 2*, particularly in the top and bottom layers.

Fig. 5 provides an overview of the model used for elastic analysis. The model consists of two rigid plates and *n* layers of boards. Rigid Plate 1 is fixed, with the radius of curvature equal to the desired inner radius of the curved glulam R_1. Rigid Plate 2 is used to press the boards into the desired shape, with a radius of curvature equal to the desired outer radius R_2, such that:

$$R_2 = R_1 + h; \qquad R_m = \frac{R_1 + R_2}{2} \tag{2}$$

where h is the height of the glulam. Based on the convergence analysis, 960 ($4 \times 4 \times 60$) twenty-node brick elements (C3D20) are assigned to each board, as shown in Fig. 5.

To save the computational effort, instead of bending each board sequentially, all boards are bent simultaneously during *Model Stages 1* and *2*, controlled by the displacement of Rigid Plate 2, such that, the distance between the two plates at the end of the two stages is set to be:

$$d_{pl}^{St1} = h; \qquad d_{pl}^{St2} = h - d_{add} \tag{3}$$

where d_{add} is the additional displacement applied to generate a constant pressure throughout the glulam, facilitating the hardening of the glue.

In reality, since each board is bent sequentially, the contact between boards is only formed when the desired curvature is reached, which means no friction can form while bending. Hence, in *Model Stages 1* and *2*, the contacts between boards, as well as the contact between the rigid plates and boards, are defined as frictionless. After the glue hardens (*Model Stage 3*), the contacts between the boards are modified to "rough contact", while the contacts between the rigid plates and boards are deactivated.

An X-symmetry plane is applied to the surface at the apex. A Cartesian coordinate system is used for each board, with the material directions L, R, and T aligned with the global directions X, Y, and Z, respectively.

The major parameters and their values for the studied case are listed below. A parameter analysis will be conducted to examine their influence on the spring-back deflection and the primary residual stress components.

- Width (w), thickness (t), and half-length of each board (l): 100 mm, 20 mm, and 1700 mm, respectively.
- Number of board layers (n): 11.
- Extra pressing displacement (d_{add}): 1‰ ×h.
- Inner radius of glulam (R_1): 2862.5 mm.

2.2. Monte–Carlo analysis for growth-ring effect

As glulam is composed of multiple layers of board, each of which is characterized by a different growth-ring pattern that is strongly related to the location in the wood logs from which the board is cut.

In order to analyze how the different growth-ring patterns influence the residual stresses, a Monte–Carlo analysis consisting of 100 simulations is conducted taking the pith location of each board as the input random variable. As suggested by [26], the statistical distribution of pith location is strongly dependent on the parameters related to the board production, such as the sawing patterns, and the harvested tree trunk diameters. Consequently, the following distribution of the pith coordinate (Y,Z) is adopted [26], as shown in Fig. 6.
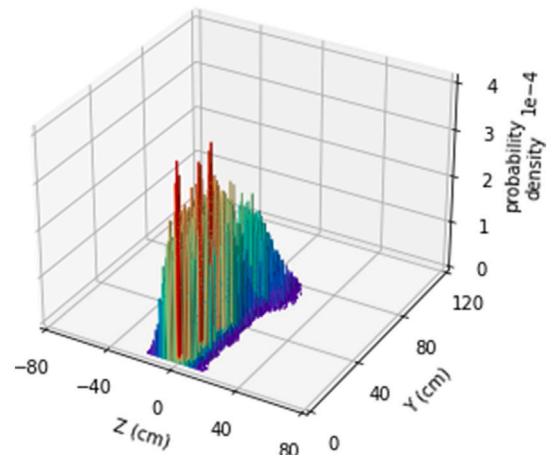

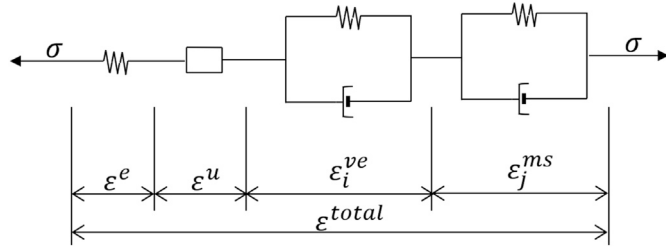**Fig. 6.** Statistical distribution of the pith coordinate.

Fig. 7. Model overview.

2.3. Time- and moisture-dependent analysis

A recent review of the development of rheological constitutive models for wood was provided in [28], where the advantages and limitations of different models are discussed. Considering the applicability to the curved glulam problem and the availability of tested parameter values, the constitutive model chosen for this work is shown in Fig. 7. This model uses the serial connect components to include the elasticity (ϵ^e), hydro-expansion (ϵ^u), viscoelasticity (ϵ_i^{ve}), and mechano-sorption(ϵ_j^{ms}). The first application of such model on wood was proposed earliest in 1971 [29] and is widely adopted in recent research works, such as [30–32].

The viscoelastic part consists of four Kelvin—Voigt components as a function of time increment (∂t).

$$\frac{\partial \epsilon_i^{ve}}{\partial t} = \frac{1}{\tau_i^{ve}} J_i^{ve} \boldsymbol{C}_0^{-1} : \boldsymbol{\sigma}_i^{ve} \tag{4}$$

where $\boldsymbol{C}_0$ is the elastic stiffness matrix at the reference moisture content ($u = 0.12$). Similarly, the mechano-sorptive component consists of three Kelvin–Voigt components as a function of the absolute change in moisture content ($\partial|u|$).

$$\frac{\partial \epsilon_j^{ms}}{\partial |u|} = \frac{1}{\tau_j^{ms}} \boldsymbol{C}_j^{ms-1} : \boldsymbol{\sigma}_j^{ms} \tag{5}$$

where the mechano-sorptive compliance matrix $\boldsymbol{C}_j^{ms-1}$ is defined as:

$$\boldsymbol{C}_j^{ms-1} = \begin{bmatrix} \frac{1}{E_L}J_{j,11}^{ms} & \frac{-\nu_{LR}}{E_L}J_{j,12}^{ms} & \frac{-\nu_{LT}}{E_L}J_{j,13}^{ms} & 0 & 0 & 0 \\ \frac{-\nu_{LR}}{E_L}J_{j,21}^{ms} & \frac{1}{E_R}J_{j,22}^{ms} & \frac{-\nu_{TR}}{E_T}J_{j,23}^{ms} & 0 & 0 & 0 \\ \frac{-\nu_{LT}}{E_L}J_{j,31}^{ms} & \frac{-\nu_{TR}}{E_T}J_{j,32}^{ms} & \frac{1}{E_T}J_{j,33}^{ms} & 0 & 0 & 0 \\ 0 & 0 & 0 & \frac{J_{j,44}^{ms}}{G_{LR}} & 0 & 0 \\ 0 & 0 & 0 & 0 & \frac{J_{j,55}^{ms}}{G_{LT}} & 0 \\ 0 & 0 & 0 & 0 & 0 & \frac{J_{j,66}^{ms}}{G_{RT}} \end{bmatrix} \tag{6}$$

$$J_{j,kl}^{ms} = \begin{cases} J_{j,L}^{ms} & kl = 11 \\ J_{j,T}^{ms} & kl \neq 11 \end{cases} \tag{7}$$

The corresponding material parameters are shown in Table 1.

Additionally, to account for moisture variation, a semi-coupled multi-field analysis is conducted using the following constitutive equation and boundary condition:

$$\frac{\partial u}{\partial t} = \nabla(\mathbf{D}\nabla u) \tag{8}$$

where diffusivity $\mathbf{D}$ is considered as moisture dependent as $D^i = D_0^i + k_D^i u$, where ($i = L, R, T$).
Boundary condition:

$$J = -\rho S_u(u - u_{EMC}) \tag{9}$$

where S_u and u_{EMC} are the surface emission coefficient and the equilibrium moisture content, respectively.

The initial moisture content of the entire beam is set to 0.12, which is the equilibrium moisture content corresponding to 20 °C and 65 % relative humidity according to Eq. (10) [33]. Based on the temperature (T) and relative humidity (RH) data provided by Deutscher Wetterdienst [34] for Munich (Germany) recorded over 365 days from February 2023 (Fig. 8), the equilibrium moisture content (u_{EMC}) can be calculated. This value is used as the film-type boundary condition on the four side surfaces along the length of the glulam.

$$u_{EMC} = 0.01 \cdot \left(-\frac{(T + 273.15) \cdot \ln(1 - RH)}{0.13 \cdot \left(1 - \frac{(T+273.15)}{647.1}\right)^{-6.46}} \right)^{\frac{1}{110 \cdot (T+273.15)^{-0.75}}} \tag{10}$$

3. Result and discussions

3.1. Analytical solution of 1D beam theory

Credited to the work of Golovin (1881) [38], whose publication in Russian remained largely unknown outside his home country, the analytical solution within the framework of linear elasticity for the stress distribution in a curved beam with a rectangular cross-section, which is subjected to a pure bending moment (M_Z), is presented by Timoshenko [39]:

$$\sigma_X = -\frac{4M_Z}{N}\left(\frac{R_1^2 R_2^2}{r^2}\log\frac{R_2}{R_1} + R_2^2\log\frac{r}{R_2} + R_1^2\log\frac{R_1}{r}\right)$$

$$\sigma_Y = -\frac{4M_Z}{N}\left(-\frac{R_1^2 R_2^2}{r^2}\log\frac{R_2}{R_1} + R_2^2\log\frac{r}{R_2} + R_1^2\log\frac{R_1}{r} + R_2^2 - R_1^2\right)$$

where:

$$N = (R_2^2 - R_1^2)^2 - 4R_1^2 R_2^2\left(\log\frac{R_2}{R_1}\right)^2$$

$$r = R_m + y \tag{11}$$

Table 1
Summary of beech wood parameters.

Elastic	E_L (MPa)	E_R (MPa)	E_T (MPa)	ν_{LR}	ν_{LT}	ν_{TR}	G_{LR} (MPa)	G_{LT} (MPa)	G_{TR} (MPa)
	1.4e4	1.9e3	6.1e2	0.28	0.23	0.28	1.3e3	8.9e2	4.9e2
Viscoelastic	τ_1 (h)	J_1^{ve}	τ_2 (h)	J_2^{ve}	τ_3 (h)	J_3^{ve}	τ_4 (h)	J_4^{ve}	
	0.82	0.15	60.86	0.123	8.90	0.088	3247.65	0.679	
Mechano-sorptive	τ_1^{ms}	$J_{1,T}^{ms}$	$J_{1,L}^{ms}$	τ_2^{ms}	$J_{2,T}^{ms}$	$J_{2,L}^{ms}$	τ_3^{ms}	$J_{3,T}^{ms}$	$J_{3,L}^{ms}$
	0.01	0.244	0.1142	0.1	0.244	0.32	1	2.013	0.0228
Diffusion & Hydro-expansion	$D_0(\frac{mm^2}{s})$	k_D	$S_u(\frac{mm}{s})$	α_L	α_R	α_T			
	4e-6	22	5.4e-4	0.011	0.191	0.462			

Notes: Elastic and viscoelastic parameters are taken from [30], which is based on [35]. The dependency of J_i^{ve} on moisture content is left out for simplicity. Mechano-sorptive parameters are from [30]. The diffusion coefficient is obtained by averaging the radial and tangential values from [30,36]. The surface emission coefficient S_u is taken as the average of radial and tangential directions from [37].
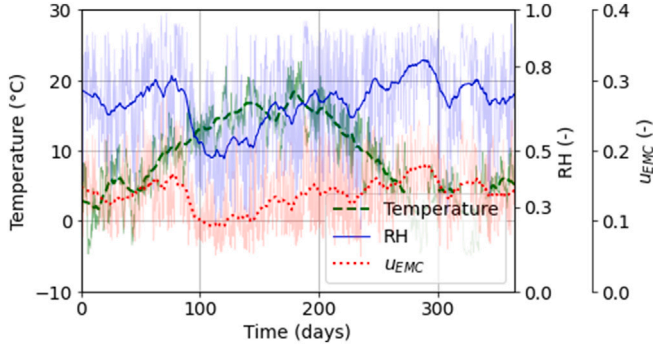
Fig. 8. Environment data.

The corresponding distribution of the stresses is as shown in Fig. 1, where the centroid axis, the neutral axis for σ_X, and the maximum location for σ_Y do not align with each other.

According to the geometry, the flexural modulus and the second moment of area of a single board and glulam are:

$$W_b = \frac{wt^2}{6}; \qquad I_b = \frac{wt^3}{12}; \qquad W_g = \frac{wh^2}{6}; \qquad I_g = \frac{wh^3}{12} \tag{12}$$

At *Stages 1* and *2*, each individual board is bent to the desired curvature. The bending moment about Z axis can be derived by the second derivative of the deflection of the beam, which in the case of constant curvature equals $\frac{1}{R_m^i}$:

$$M_Z^{St1,i} = M_Z^{St2,i} = \frac{E_L I_b}{R_m^i} \tag{13}$$

where $R_m^i = R_1 + t\left(i - \frac{1}{2}\right)$ is the middle radius of ith layer of board.

At *Stage 3*, as shown in Fig. 4, spring-back occurs due to the removal of the bending moment from *Stage 2*.

Hence, this stage can be simplified as applying a bending moment $-M_Z^{ST3}$ to the whole glulam, which is the inverse of the sum of all the bending moments on each individual board from *Stage 2*:

$$-M_Z^{St3,N} = -\sum_{i=1}^{n} M_Z^{St2,i} = -\sum_{i=1}^{n} \frac{E_L I_b}{R_m^i} \tag{14}$$

For $\frac{h}{R_m} \leq 10$:

$$-M_Z^{St3,N} \approx -\frac{nE_L I_b}{R_m} \tag{15}$$

as the relative difference is less than 0.1 %.

Substitute the moments into Eq. (11), the stress distribution of different stages along Y axis can be derived in Fig. 9. The longitudinal stress at *Stage 2* is the same as *Stage 1*, while the radial stress at *Stage 2* would be the stress at *Stage 1* plus a constant pressure along Y axis due to the additional pressure caused by d_{add}. $-M_Z^{St3,N}$ is in the same direction as the bending moment that will be applied later when the beam is in service. Hence, the parts of residual stress which are from the spring-back effect, σ_X^{Nett} and σ_Y^{Nett}, will act in the same direction as the ones from service load, with the same location for the maximum value. In contrast, the residual stress from M_Z^{St1} is in the opposite direction to the stress generated by the service moment. However, since each board acts individually, the distribution is not the same. As a result, radial stress σ_Y^{St1} has little influence on the final stress from service load, while the longitudinal stress σ_X^{St1} would add up to both the maximum tension and compression from service load, as shown in Fig. 9.
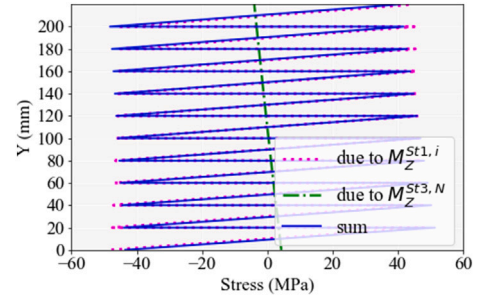
(a) longitudinal stress σ_X
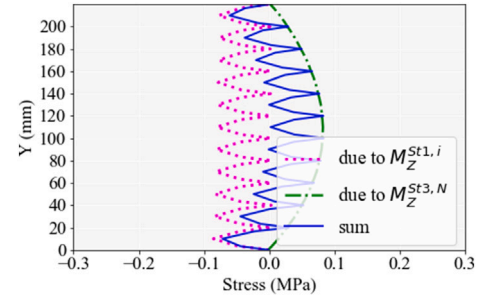
(b) radial stress σ_Y

Fig. 9. Analytical solution of stress distribution along Y axis.

3.2. Stress development from elastic FE analysis

Contact Pressure

Fig. 10 shows the development of the contact pressure at the end of *Stages 1* and *2* when the d_{add} is set to be 1‰ of the total beam height (h).

First, it has to be noted that at the end of the beam, the contact pressure is much higher than the expected material strength. Such "unreasonably high" stress is due to the adoption of *Saint-Venant's Principle* in the FE model. In the model, both the molds are set to have a constant radius, which means a constant bending moment is required for the whole length. To achieve this, the force required is concentrated in a small area at the beam end. However, in reality, the curvature at the end of the beam is usually flattened in a more smooth manner. According to *Saint-Venant's Principle*, such a modeling method is reasonable when the interest of the research is focused on the part that is sufficiently far, such as the apex region. Consequently, the stresses at the beam shall not be discussed.

As for the apex region, it can be seen that the contact pressure is concentrated at the two borders of the top surface, which is consistent with the analysis in Fig. 4 (red circles). Fig. 12 shows the correlation between the contact pressure and the additional displacement of the top plate (d_{add}). As the material is set to be linearly elastic, linear correlation can also be observed, with the slope equal (with small deviation) to the radial elasticity for $\frac{d_{add}}{h} \geq 0.5$‰. Unless otherwise specified, all following results shown in this work are for the condition $\frac{d_{add}}{h} \geq 1$‰.

Additionally, the anticipated cup deformation can clearly be observed at *Stage 1*. At *Stage 2*, although the top and bottom surfaces are flattened by the plates, slight cup deformation can still be observed in the middle boards. At *Stage 3*, as spring-back occurs, the cup deformation also partially recovers, but with a smaller curvature compared to *Stage 1*. These observations are crucial for analyzing the development of transverse stresses, as shown below.

Longitudinal Stress (σ_X)

From Fig. 13(a) it can be seen that the longitudinal stress at the cross section at the apex is constant along the Z direction, and only a slight difference can be observed between *Stage 3* and *Stage 2*.
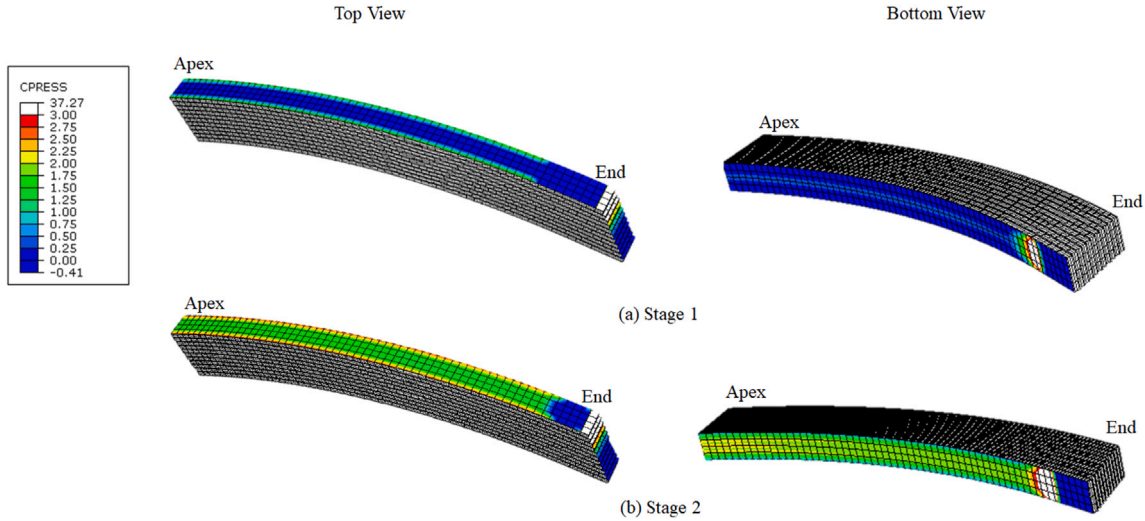
Fig. 10. Contact pressure at different stage.
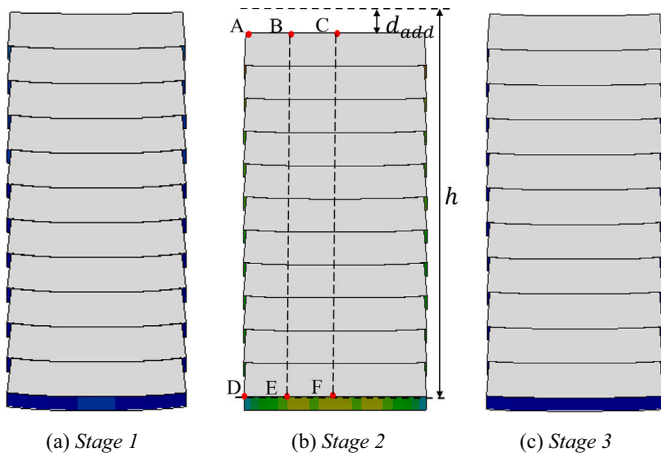

(a) *Stage 1* (b) *Stage 2* (c) *Stage 3*

Fig. 11. Deformation of the cross section at apex (with scale factor of 50).
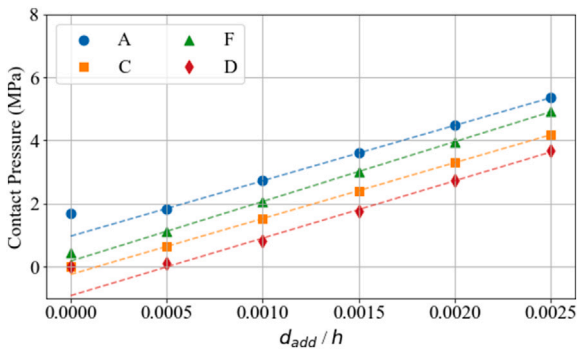
Fig. 12. Contact pressure vs d_{add} at the four locations (marked in Fig. 11).
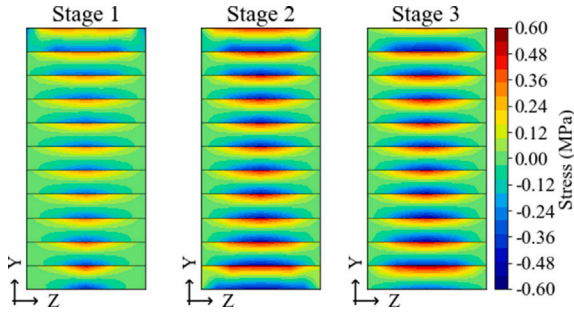

(a) σ_X in the cross section

Note: $\sigma^{St2,N} = \sigma^{St2} - \sigma^{St1}$, $\sigma^{St3,N} = \sigma^{St3} - \sigma^{St2}$
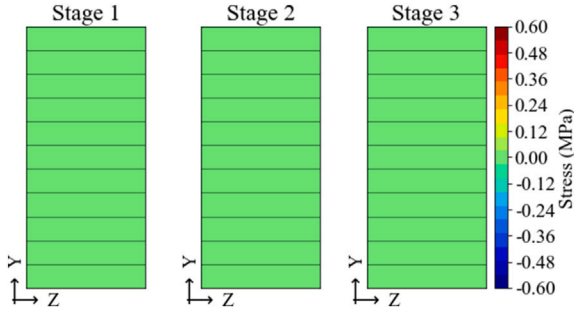
(b) σ_X along the middle path CF (see Figure 11)

Fig. 13. Longitudinal stress σ_X at the apex.

For better visualization of the stress difference at different stages, the stress along the middle path (path CF in Fig. 11) is shown in Fig. 13(b). The net stress $\sigma^{Sti,N}$ represents the stress difference between *Stage i* and its previous stage. The non-zero $\sigma^{St3,N}$ can be contributed to the bending moment $-M_Z^{St3,N}$ from the spring-back effect. The development and distribution match the longitudinal stress derived from Section 3.1.
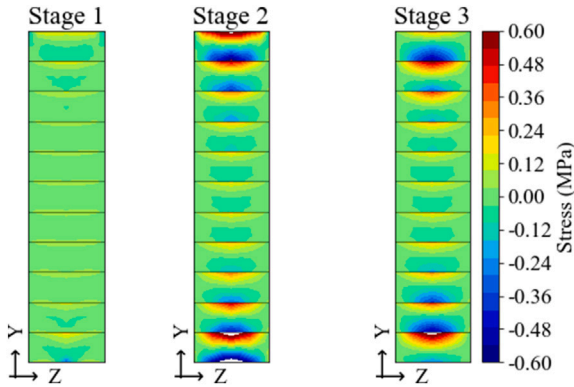
Z-direction Stress (σ_Z)

The distribution of the simulated tangential stress (corresponding to Z axis) in Fig. 14(a) from the three stages shares the common feature, such that there is tension on top of the board and compression on the bottom. Comparing the stress to the deformation in Fig. 11, it can be deduced that the stress is related to the cup deformation. In addition, this can also be confirmed by zero stress shown in Fig. 14(b), where the Poisson's ratio v_{TL} is modified to zero.

(a) $t = 20$ mm, v_{TL} from Table 1

(b) $t = 20$ mm, $v_{TL} = 0$

(c) $t = 40$ mm, v_{TL} from Table 1

Fig. 14. Z direction stress σ_Z in the cross section at the apex.

(a) σ_Y when v_{TL} from Table 1

(b) σ_Y^{NPo} when $v_{TL} = 0$

(c) σ_Y^{Po} as the difference between (a) and (b)

Fig. 15. Y direction stress σ_Y in the cross section at the apex.

- σ_Y^{NPo} in Fig. 15(b) is the part where Poisson's ratio v_{TL} is assumed to be 0.
- σ_Y^{Po} in Fig. 15(c) relates to the cupping deformation in the transverse direction caused by the Poisson's ratio.

Fig. 16(a) shows σ_Y^{NPo} along the middle path of the cross section. The matching of Fig. 16(a) and Fig. 9(b) confirms the analysis of Section 3.1 that the stress at *Stage 3* is composed of a part due to spring-back effect (corresponding to the bending moment $-M_Z^{St3,N}$) and a part due to the curving of each board (corresponding to bending moments $M_Z^{St1,i}$).

As for σ_Y^{Po}, Fig. 15 (c2) shows that it primarily occurs along the two sides of the beam at *Stage 2*, aligning with the expected red circles in Fig. 4. Additionally, a gradual transition from compression at the top to tension at the bottom is observed. This trend persists in *Stage 3*, except for slight "spring-back" effects at the very top and bottom layers.

Furthermore, Fig. 16(b) presents a linear trend line for the Y-direction stress at both stages, revealing that they share the same slope. To understand the formation of this constant slope, the underlying mechanism of Z-direction stress in Fig. 4 must be considered:

From *Stage 1* to *Stage 2* the curvature in the Z direction is being flattened. This can be viewed as applying an inverse bending moment (M_X^i). However, since there are no external forces (i.e., forces that act from the outside the whole glulam) at *Stage 2*, the moment for each ith layer is generated by the vertical forces received from its upper (F_Y^{i+1}) and bottom (F_Y^{i-1}) neighboring layers, such that $F_Y^{nett} = F_Y^{i-1} - F_Y^{i+1}$.
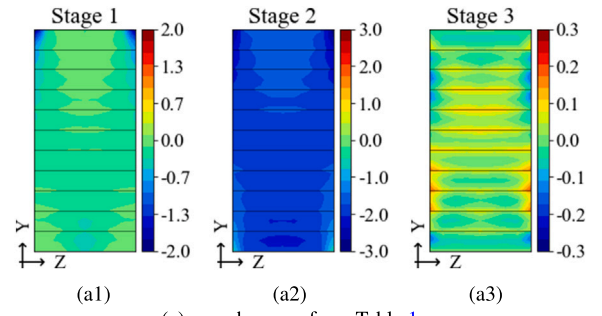
At *Stage 2*, particularly in the top and bottom boards, the Z-direction stress is more pronounced along the whole width of the cross-section. This occurs because the top and bottom boards are almost completely flattened by the press, as $d_{add} = 1‰ h$. The reduced width caused by cupping on the top surface is stretched, creating tension. Conversely, the opposite effect occurs on the bottom surface. It can also be seen from Fig. 11(b) that the "flatting" effect is gradually reduced towards the inner layers. As shown in Fig. 11(c), when the dimension ratio of board $\frac{t}{w}$ increases, the reduction becomes more drastic.

The major difference between *Stage 3* and *Stage 2* is only the top and bottom surfaces of the glulam, as the removal of press frees the cupping deformation at surfaces. Yet, due to the solidified glue, the deformation in the inner layers remains nearly unchanged from *Stage 2*.
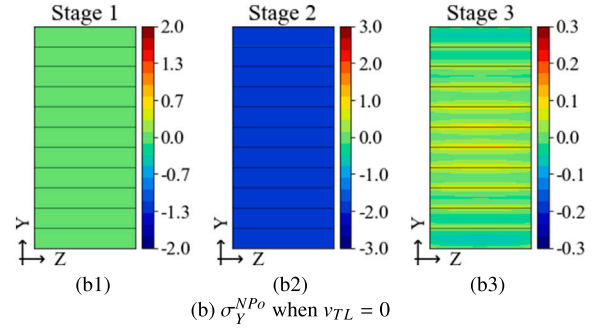
However, it is noticed that unlike the longitudinal stress (in Fig. 13), the Z-direction stress is never uniform along the entire width (Z) direction. This is related to the formation mechanism of the Y-direction stress which will be explained in the next section.
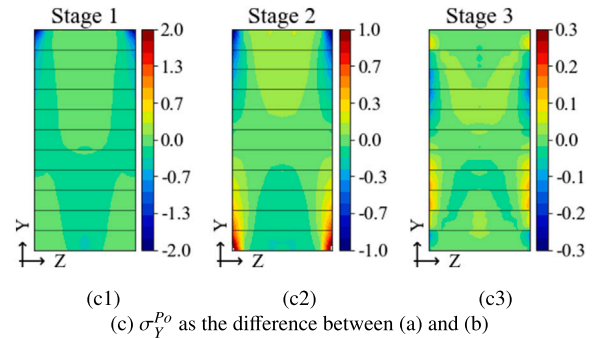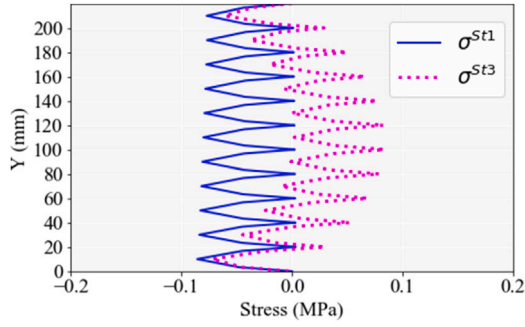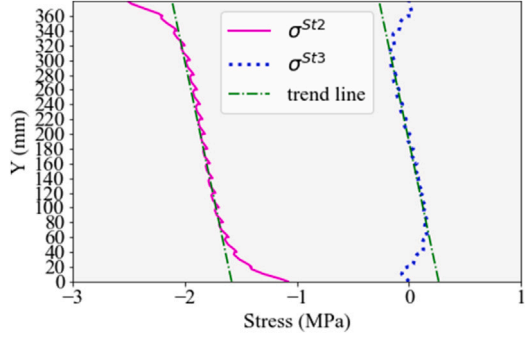
Y-direction Stress(σ_Y)

Fig. 15(a) shows the Y-direction stress during the 3 stages, which can be decomposed into two parts:

(a) σ_Y^{NPo} along the middle path CF (see Figure 11)

(b) σ_Y along the side path AD (see Figure 11) for a 19-layer glulam
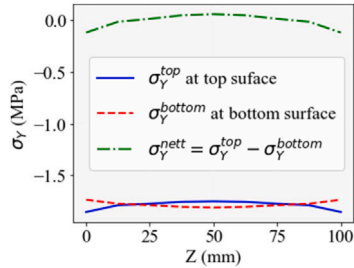
(c) σ_Y along Z direction at *Stage 2* in the fifth layer

(d) F_Y along Z direction at *Stage 2*

(e) M_X along Z direction at *Stage 2*

Fig. 16. Analysis of stress σ_Y.

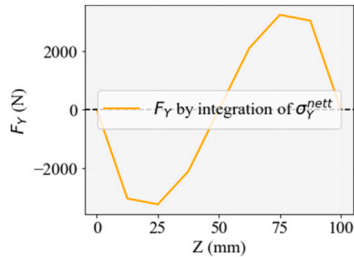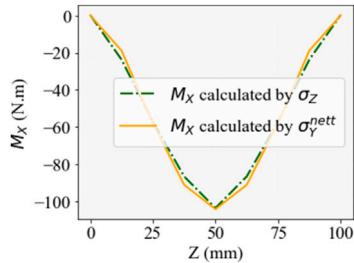Since the moment needed for each layer M_X^i is almost the same among different layers, F can be considered uniform among different layers. Consequently, a uniform slope can be expected.
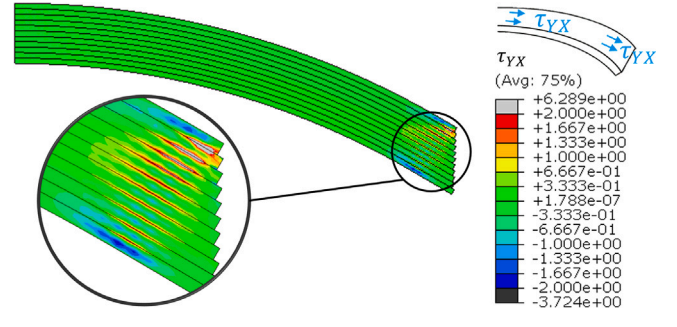

Fig. 17. Residual shear stress $\tau_{YX}^{residual}$.

Taking the fifth layer as an example, Fig. 16(c) shows the net Y-direction stress σ_Y^{nett} at *Stage 2*. Fig. 16(e) shows the M_X derived from the two following methods:

- M_X derived from σ_Y^{nett}:

$$F_Y^{nett} = \int_0^w (\sigma_Y^{nett} \times 2l) dz \qquad (16)$$

$$M_X^{\sigma_Y^{nett}} = \int_0^w F_Y^{nett} dz \qquad (17)$$

- M_X derived from σ_Z:

$$M_X^{\sigma_Z} = \frac{\sigma_Z I_X}{\frac{t}{2}} \qquad (18)$$

where $I_X = \frac{(2l)t^3}{12}$ is the second moment of area about X axis.

The above explanation is validated by the good alignment of the moment M_x derived from these two methods in Fig. 16(e). Additionally, the question from the previous section—why σ_Z is not uniform along the Z direction—can also be explained, as the moment M_X which results in σ_Z and which is formed by the second integration of σ_Y^{net} is not constant along the Z direction.
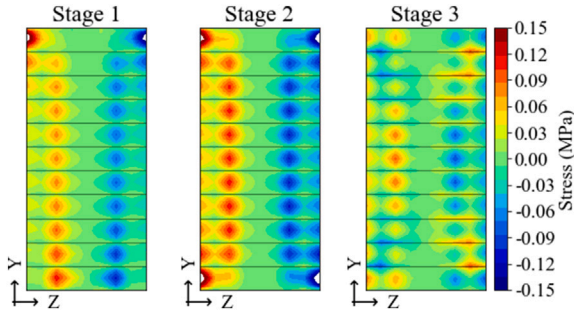
Shear Stress τ_{YX}

Fig. 17 shows the simulated residual shear stress τ_{YX} at *Stage 3*. It can be seen that for most of the beam region, the shear stress τ_{YX} remains zero. This is due to the constant radius of curvature, which means constant $\frac{d^2\omega}{dx^2}$ and no change in the required bending moment $M_Z^{St1,i}$.

In contrast, at the end of the beam, the required bending moment drastically changes from zero to the required value corresponding to the constant curvature. In order to form the moment, a high concentration of τ_{YX} is observed. However, as explained before, such a drastic change in the moment is only due to the adoption of Saint-Venant's Principle in the FE model. Hence, the high shear stress at the beam end is to be expected in the model and does not influence the validity of stress analysis of the major part of the beam, especially at the apex.

Shear Stress τ_{YZ}

Fig. 18 shows the simulated shear stress τ_{YZ} at different stages at the apex. From the zero value in the case when v_{TL} is set to be zero (Fig. 18(b)), it can be seen that the formation of the τ_{YZ} is also related to the cupping deformation caused by the Poisson's effect.

At *Stage 2*, it can be seen that the shear stress τ_{YZ}^{St2} is positive on the left side and negative on the right side. This is aligned with the distribution of the Y-direction force F_y in Fig. 16(d) that is caused by the bending moment M_X at *Stage 2*. Also, the distribution of τ_{YZ}^{St2} along the Y direction in each board can also be explained by the classic beam theory as shown in Fig. 18(c).

(a) τ_{YZ} when v_{TL} from Table 1
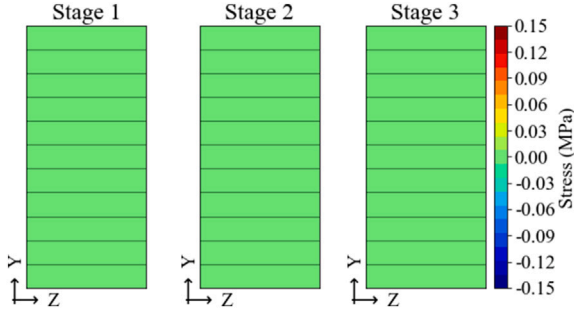
(b) τ_{YZ} when $v_{TL} = 0$

(c) formation mechanism of τ_{YZ} due to F_Y in Figure 16 (d)

Fig. 18. Shear stress τ_{YZ} in the cross section at the apex.

At *Stage 3*, compared to *Stage 2*, the τ_{YZ} inside each board gets reduced, while a new type of shear between the interfaces of boards can be observed. This is because after removing the pressure from the rigid plates, the bending moment M_X in the top and bottom layers cannot be maintained solely by the $\sigma_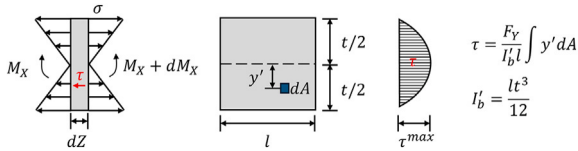Y^{net}$. Hence, the contribution of the shear stress at the interface is needed. This is also the reason why this type of τ_{YZ}^{St3} is mainly exhibited at interfaces between the most outer layers, where the σ_Y^{St3} deviates from the linear trend line, as shown in Fig. 16(b).

3.3. Parametric analysis

From the above analysis, it can be seen that there are two major causes of all the stress during manufacturing. The first is related to the bending moment above the Z axis, including $M_Z^{St1,i}$ for curving each board and $-M_Z^{St3,N}$ due to the spring-back effect. The second cause is related to the flatting of the cupping deformation in the transverse direction and, hence, related to the bending moment $-M_X$ above the X axis. Hence, figuring out the parameters that influence these bending moments is the key to identifying the parameter that influences the corresponding residual stresses.

3.3.1. Parameters related to M_Z

The stresses caused by M_Z are mainly the longitudinal stress σ_X and the part of Y-direction stress when excluding Poisson's effect σ_Y^{NPo}. These stresses can be well estimated analytically.

Based on the work of Moehler and Blumer [40] along with Ehlbeck et al. [41], the following simplified equations are adopted in the current design standards such as Eurocode 5 [12], to estimate the maximum longitudinal stress σ_X and perpendicular-to-grain stress σ_Y in curved beams:

$$\sigma_{X,\max} = \left[1 + 0.35\frac{h}{R_m} + 0.555\left(\frac{h}{R_m}\right)^2\right]\frac{M}{W}$$
$$\sigma_{Y,\max} = \left(0.25\frac{h}{R_m}\right)\frac{M}{W} \tag{19}$$

According to the $M_Z^{St1,i}$ and $-M_Z^{St3,N}$ obtained in Eqs. (13) and (15), it can be derived that the max longitudinal stress from these two parts can be estimated as (for $n \geq 3$ and $\frac{nt}{R_m} \leq 10$):

$$\sigma_{X,\max}^{St1} \approx \frac{E_L t}{2R_m} \tag{20}$$

$$\sigma_{X,\max}^{St3,N} \approx \frac{E_L t}{2R_m}\left(\frac{n-2}{n^2}\right) \tag{21}$$

As shown in Fig. 13, the final maximum longitudinal stress $\sigma_{X,\max}^{St3}$ is approximated the sum of the $\sigma_{X,\max}^{St1}$ and $\sigma_{X,\max}^{St3,N}$, and can be estimated as $\frac{E_L t}{2R_{inner}}\left(1 + \frac{n-2}{n^2}\right)$, as shown in Fig. 19.

Additionally, from Eqs. (20) and (21), $\frac{n-2}{n^2}$ corresponds to the ratio between $\sigma_{X,\max}^{St3,N}$ and $\sigma_{X,\max}^{St1}$, which can be considered as the influence level of the spring-back effect on the maximum residual stress. From Fig. 20, it can be seen that for $n \geq 4$, the lower the number of the layers, the stronger the influence from the spring-back effect, and the highest influence can be up to 12.5 %.

However, as shown in Eq. (1), Eurocode 5 [12] only considers the influence of $\frac{t}{R_m}$ on the residual longitudinal stress, yet the influence of the spring-back effect (dependent primarily on $\frac{n-2}{n^2}$) is not covered.
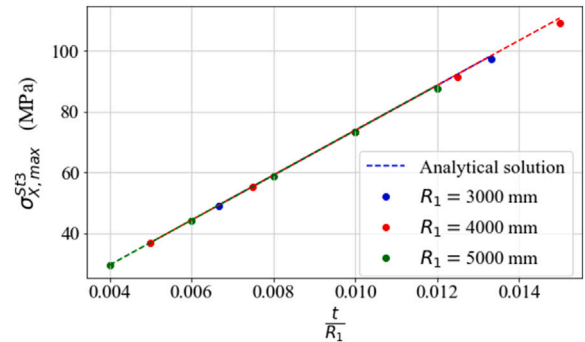

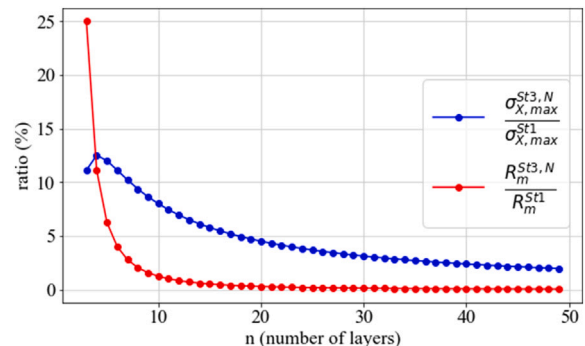**Fig. 19.** Parameter analysis of $\sigma_{X,\max}^{St3,N}$.

Fig. 20. Influence of spring-back on the residual stress ($\sigma_{X,\max}^{St3,N}/\sigma_{X,\max}^{St1}$).

Similarly, it can be deduced that the part of the maximum residual Y-direction stress σ_Y^{NPo} is linearly related to $\frac{E_t}{R_m}$, as it equals the maximum of the Y-direction stress caused by the spring-back moment $-M_Z^{St3,N}$, as shown in Fig. 9(b).

Additionally, according to Eq. (15), the corresponding deflection ($\omega^{St3,N}$) caused by the spring-back can be calculated as:

$$\frac{d^2\omega^{St3,N}}{dx^2} = \frac{-M_Z^{St3,N}}{E_L I_g} \approx -\frac{1}{n^2 R_m} \tag{22}$$

Consequently, the relative change in the radius after and before spring-back:

$$\frac{R_m^{St3}}{R_m^{St1}} = \frac{n^2}{n^2 - 1} \tag{23}$$

which is only influenced by the number of layers n, as shown in Fig. 20.

3.3.2. Parameters related to M_X

The residual stress components related to M_X - the inverse bending of the transverse cupping deformation caused by Poisson's effect - are σ_X, σ_Y^{Po} and τ_{YZ}. According to Fig. 4,

- **Stage 1**:
  for each board, the longitudinal stress σ_X is generated due to fiber elongation or shortening (ε_X) related to bending deformation. Due to Poisson's ratio (ν_{LT} when the material T corresponds to the global Z direction), longitudinal strain ε_X induces strain in the Z direction if the cross-section can deform freely:

$$\varepsilon_Z^{cup} = -\nu_{LT}\varepsilon_X = -\nu_{LT}\frac{\sigma_X}{E_L} \tag{24}$$

- **Stage 2** and **Stage 3**:
  due to the pressure from the press, the curvature at *Stage 1* got flattened, which can be viewed as applying a strain of $-\varepsilon_Z^{cup}$. Hence, the corresponding stress can be deduced:

$$\sigma_Z = -\varepsilon_Z^{cupping} E_T = \frac{\nu_{LT} E_T}{E_L}\sigma_X \tag{25}$$

As a result, it can be deduced that, besides the dependency on parameters that control σ_Z^{St1}, which is $\frac{E_L t}{R_m}$, the residual transverse stress σ_Z^{St3} shall be influenced also by $\frac{\nu_{LT} E_T}{E_L}$, as shown in Fig. 21.

Fig. 21(b) shows a good agreement between the simulated results and the analytical solution for the case when the dimension ratio of the individual board $\frac{t}{w} \leq 0.3$. Beyond this range, the deviation between them increases for larger $\frac{t}{w}$. This is because Eq. (25) is derived on the basis that, from *Stage 1* to *Stage 2*, the board can be considered as a slender beam along the Z direction. Yet, this assumption does not hold when $\frac{t}{w}$ becomes larger. As a result, the distribution of stress inside each board becomes non-linear as shown in Fig. 14(c).

Similarly, it can be deduced that $\frac{E_L t}{R_m}$ and $\frac{\nu_{LT} E_T}{E_L}$ also influence σ_Y^{Po} and τ_{YZ}.

Furthermore, since the σ_Y^{nett} is constant in each layer, the residual stress σ_Y^{Po} shall get larger as the number of layers increases, as can be seen in Fig. 22.

As a result, Table 2 summarizes the relevant geometric and material parameters that can influence residual stresses. Besides the already known parameters E_L, t, and R_m, it can be seen that the number of layers n and material parameter $\frac{\nu_{LT} E_T}{E_L}$ are also important.

3.4. Growth-ring effect

Fig. 23 shows the stress in the three principle directions in two examples where the pith location of each board layer is assigned using the random variable according to the distribution in Fig. 6.
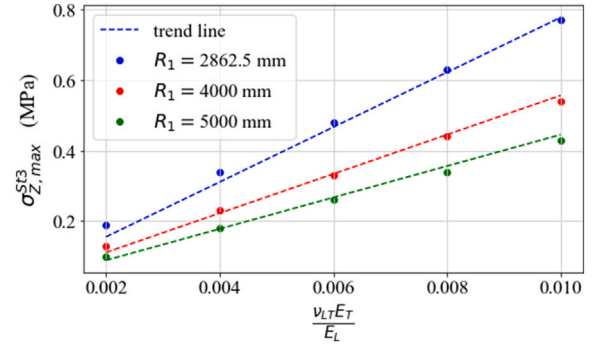
(a) correlation with $\frac{\nu_{LT} E_T}{E_L}$
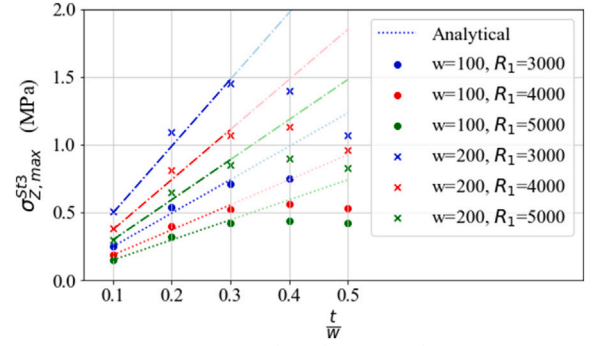
(b) correlation with board thickness t

Fig. 21. Parameter analysis of $\sigma_{Z,max}^{St3}$.
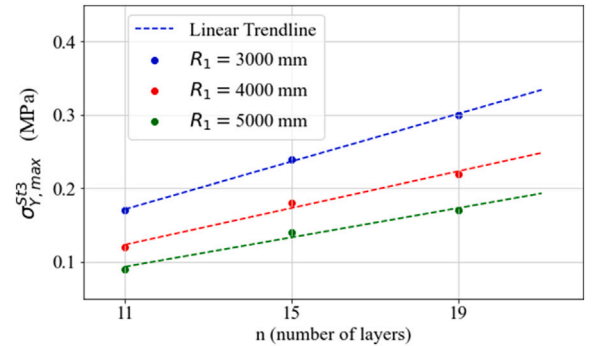
Fig. 22. $\sigma_{Y,max}^{St3}$ vs n.

Table 2
Summary of the parameter analysis under elastic range.

	R_m	t	n	E_L	$\frac{\nu_{LT} E_T}{E_L}$
$\frac{R_m^{St1}}{R_m^{St1}}$			↓		
σ_X^{max}	↓	↑	↓	↑	
σ_Z^{max*}	↓	↑		↑	↑
σ_Y^{NPo}	↓	↑		↑	
σ_Y^{Po**}	↓	↑	↑	↑	↑
τ_{YZ}	↓	↑		↑	↑

* The relationship is valid under the condition that $t/w \leq 0.3$.
** The relationship is valid under the condition that $t/w \leq 0.3$ and $n \geq 11$.

Comparing the stress in the two examples with the result in Fig. 23(a) where the growth-ring effect is not considered (referred to as *Standard Case* in the following), it can be seen that stress in the longitudinal direction is not influenced by varying the pith location, yet, strong deviations are present in both radial and tangential directions.

(a) *Standard Case* (no growth-ring effect is considered)

(b) Example 1

(b) Example 2

Fig. 23. Stress in R, T, L direction at *Stage 3* (Unit: MPa).

Fig. 24. Distribution of the maximum stress of each layer from 100 cases.

Fig. 25. Distribution of the all maximum stresses in Layers 3–8.

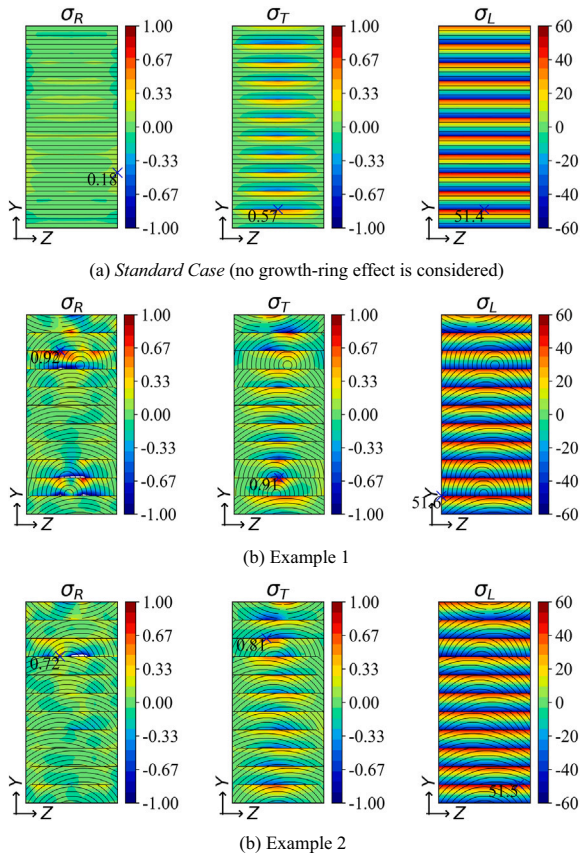Unlike in Fig. 23(a) where the radial stress σ_R^{St3} (corresponding to global σ_Y^{St3}) is much smaller than tangential σ_T^{St3} (corresponding to global σ_Z^{St3}), these two stress components are in the same magnitude range in the cases when growth-ring is considered, since the higher global σ_Z^{St3} is carried by both local radial and tangential directions, dependent on the pith direction.

Moreover, the location of maximum stress for both radial and direction is also varied from *Standard Case*, with also higher magnitude.

Fig. 24 shows the histogram of the maximum tangential and radial stresses of each layer from 100 simulations, which were selected based on a convergence analysis according to the following criterion:

$$\text{Relative Error} = \frac{|\text{Current Estimate} - \text{Final Estimate}|}{|\text{Final Estimate}|} < 0.05 \qquad (26)$$

It can be seen that for both tangential and radial cases, the distribution of the maximum stresses in the top layers (Layers 10 and 11) exhibit the highest median and 95-percentile values. This is due to the flipping board direction.

In contrast, the distribution of maximum stresses for most of the inner layers (Layers 3–8) is very similar. In consideration of the influence of the later bending stress from the service load, whose maximum is mainly presented in the middle layers, the distribution of the maximum residual stress of the inner layers is of the main interest, and the summary of all the maximum values from these inner layers is plotted in Fig. 25.

The distribution of the tangential and radial stresses differs from each other, as the pith location is not chosen as uniform random variables but according to the cutting pattern as shown in Fig. 6. By comparing the median value of the maximum stress to the one from *Standard Case*, it can be seen that no less than half of the scenarios, a higher maximum stress than the maximum of the *Standard Case* will be exhibited. From
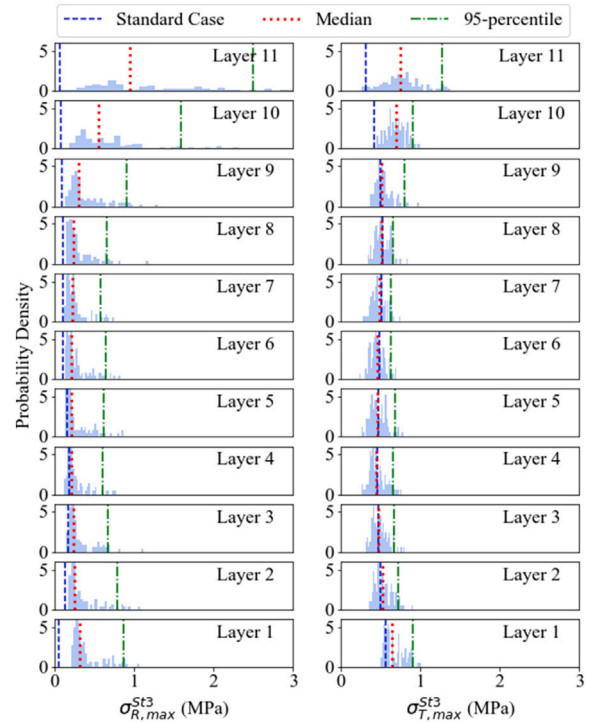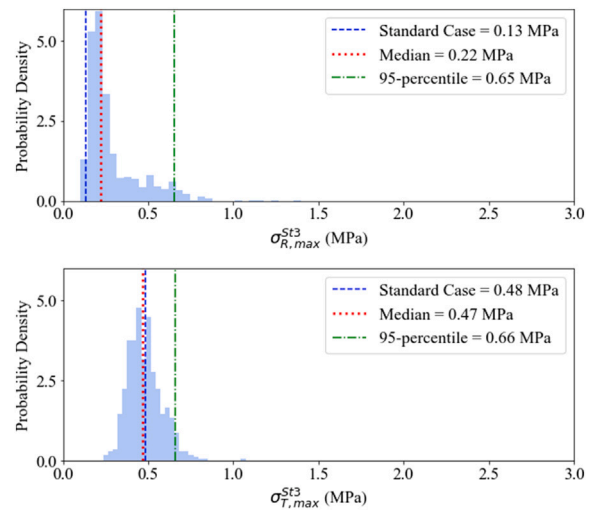
the practical point of view, the 95th percentile value shall be taken into account for the safety analysis, which is around 0.66 MPa for both tangential and radial directions, around 1.4 times of maximum X direction stress from *Standard Case*. This stress will then be added up with the bending stress caused by the service load. As suggested by [42,43], the combination of different stress components can trigger earlier damage or failure.

The current approach employs a two-dimensional probability density function to characterize the spatial variation in pith location. In contrast, studies such as [44–46] utilize random field models, which account for spatial correlations in material heterogeneity—such as variations in strength and stiffness—both within individual boards and across adjacent ones. Furthermore, it is important to emphasize that the stress

(a) Stress development in 7 days

(b) Relative Relaxation in 600 days

Ai: i^{th} layer, upper node A
ai: i^{th} layer, lower node a

Fig. 26. Stress relaxation under constant T and RH.

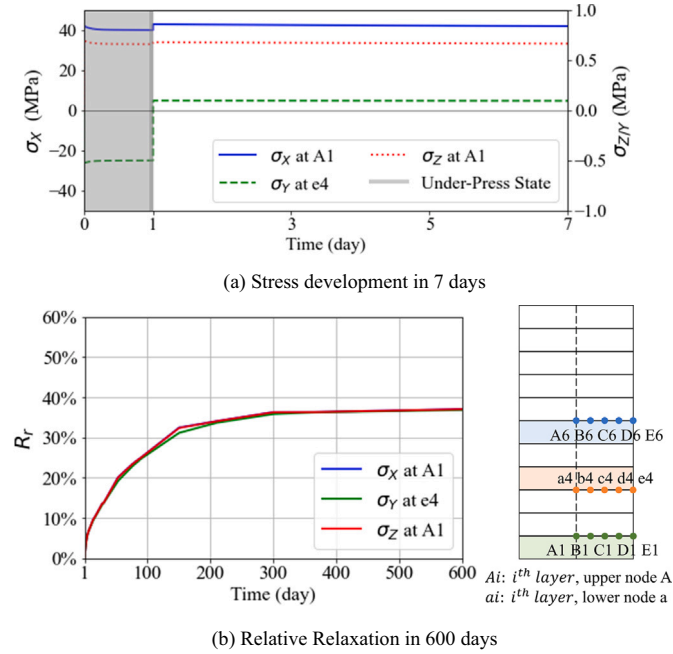conditions in a glulam beam differ from those in standardized, quality-controlled test specimens. As highlighted in [47,48], the stress state in real glulam structures involves a combination of stress types that are not fully represented in laboratory testing.

3.5. Time- and moisture-dependent relaxation

3.5.1. Viscoelastic relaxation

Fig. 26 illustrates the stress evolution under constant moisture content to analyze the contribution of the viscoelastic component. The locations for stress measurement are chosen at the points of maximum residual stress: the top center of the lower first board for σ_X and σ_Z, and the bottom right of the lower fourth board for σ_Y. Fig. 26(a) shows the stress development over the first 7 days. It is evident that relaxation begins during the Under-Press State. To compare the percentage of relaxation of different stress components, the relative relaxation (R_r) is

calculated using the following equation:

$$R_r(t) = 1 - \frac{\sigma(t)}{\sigma_0} \tag{27}$$

where σ_0 is defined as the stress value at $t = 1$ day.

Fig. 26(b) shows the relaxation due solely to viscoelasticity. The data indicate that relaxation reaches its maximum after around 300 days. According to EC5 [12] Table 3.2, the k_{def} value for Service Class I is 0.6, resulting in $R_r^{EU5} = 1 - \frac{1}{1+k_{def}} = 0.375$, which aligns well with the simulated value $R_r^{ve} = 37\%$.

It is important to mention that the constitutive model in this study assumes a uniform J^{ve} value for all three material directions. The assumption is made due to the complexity of the constitutive model and the limited availability of tested parameters. This assumption results in identical viscoelastic relaxation curves for the three stress components, as shown in Fig. 26(b). Future research could explore the development of viscoelastic models incorporating orthotropic J^{ve} values and time-dependent Poisson's ratios, as discussed in [49].

Fig. 27 illustrates the moisture content fluctuations at various locations within glulam beams made of different widths (dimension ratio $\frac{t}{w} = 0.2$) and wood species. Notably, for beams with a 100 mm width, the center point (represented by point A5) exhibits significant fluctuations, whereas beams with a 700 mm width show nearly constant moisture content at the center point over time.

In order to isolate the relaxation effect from the shrinkage stress caused by the moisture fluctuations, two simulation cases were conducted. The first case was conducted on a curved beam and the second case on a straight beam. The difference in the stress between these two cases is considered to be the net residual stress and is presented in the following analyses.

Fig. 27 also shows the relative relaxation (R_r) of longitudinal residual stress (σ_X^{St3}) at various locations in a glulam beam under fluctuating T and RH. At the center (A6) surface (E6) points, the relaxation is 63% and 76%, respectively.

When comparing these values to the relaxation due purely to viscoelasticity (37%), it is evident that mechano-sorptive relaxation is a significant factor. Furthermore, 76% can be considered the upper limit for relaxation, with the potential for all locations within the beam to eventually reach this value given sufficient time. This relaxation limit is also higher than the one estimated by EC5 [12]. According to EC5 Table 3.2, $k_{def} = 2$ for Service Class III, resulting in $R_r^{EU5} = 1 - \frac{1}{1+k_{def}} = 0.667$, suggesting that EC5 could have underestimated the creep effect.
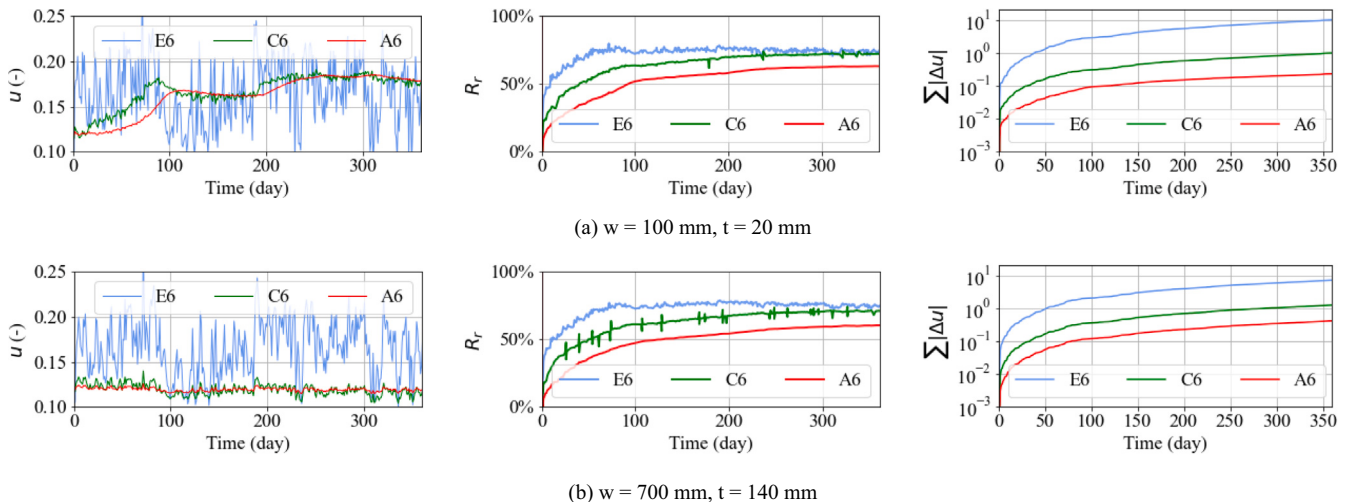

(a) w = 100 mm, t = 20 mm

(b) w = 700 mm, t = 140 mm

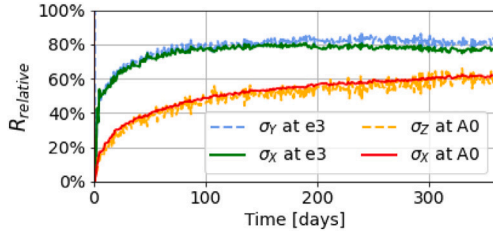**Fig. 27.** Moisture and relaxation under fluctuating T and RH.

Fig. 28. Relative relaxation (R_r) of different stresses type.

Interestingly, despite the significant differences in moisture fluctuations observed in Fig. 27, the difference in relative relaxation (R_r) between the 100 mm and 700 mm glulam beams is relatively small ($\leq 6\%$).This small difference can be attributed to the nature of mechano-sorptive strain, which depends on the absolute moisture change ($|\Delta u|$) rather than the directional moisture change (Δu), as described in Eq. (5). Therefore, although the moisture content at the center point (A6) of the 700 mm glulam beam remains nearly constant, the total sum of absolute moisture changes ($\sum |\Delta u|$) is not significantly different from that of the 100 mm glulam beam, as shown in Fig. 27.

From Fig. 28 it can be seen that the relaxation of different stress types at the same point tends to align, despite the fact that the longitudinal mechano-sorptive parameter $J_{j,11}^{ms}$ is different from the transverse $J_{j,22}^{ms}$ and $J_{j,33}^{ms}$, as shown in Table 1. This alignment can be understood by referring to the formation mechanism of transverse residual stresses. The residual stresses (σ_Y^{St3} and σ_Z^{St3}) are closely related to the longitudinal stress and Poisson's ratio, as given by the following equation:

$$\sigma_Y^{St3} \propto \sigma_Z^{St3} \propto \sigma_X^{St3} \frac{v_{LT} E_T}{E_L} \tag{28}$$

After relaxation (abbreviated as "St4"), the relationship becomes:

$$\sigma_Z^{St4} \propto \sigma_X^{St4} \frac{\left(\frac{v_{LT}}{E_L}\right)^{St4}}{\left(\frac{1}{E_T}\right)^{St4}} \propto \sigma_X^{St4} \frac{f(J_{j,13}^{ms})}{f(J_{j,33}^{ms})} \tag{29}$$

Here, $f(J_{j,13}^{ms})$ and $f(J_{j,33}^{ms})$ are functions derived from the mechano-sorptive creep compliance tensors $J_{j,13}^{ms}$ and $J_{j,33}^{ms}$, as described by the heredity integral approach in [28]. Since the model assumes $J_{j,13}^{ms} = J_{j,33}^{ms}$, it simplifies to:

$$\sigma_Z^{St4} \propto \sigma_X^{St4}, \quad \sigma_Y^{St4} \propto \sigma_X^{St4} \tag{30}$$

This indicates that the similar R_r values observed in both transverse and longitudinal directions in Fig. 28 come from the assumption $J_{j,13}^{ms} = J_{j,33}^{ms}$ in the mechano-sorptive model used in this study.

However, it needs to be mentioned that this assumption requires further validation. One potential issue with this assumption is that it leads to a time-dependent Poisson's ratio, as expressed by:

$$\left(\frac{v_{LT}}{E_L}\right)^{St4} \propto f(J_{j,13}^{ms}) = f(J_{j,33}^{ms}) \tag{31}$$

$$\left(\frac{1}{E_L}\right)^{St4} \propto f(J_{j,11}^{ms}) \tag{32}$$

Since $J_{j,33}^{ms} \neq J_{j,11}^{ms}$, this implies that v_{LT} is not constant when mechano-sorption occurs. In contrast to the time-dependent behavior in viscoelasticity, which has been identified and characterized through various experiments [50,51], studies on the change of Poisson's ratio during mechano-sorption are limited. This is largely due to the experimental difficulty in capturing off-axis compliance components $J_{j,ij}^{ms}$, which require precise control over load, moisture, and time, as well

as accurate pre-characterization of other parameters such as hygro-expansion and axial compliance $J_{j,ii}^{ms}$. Additionally, the assumption of a constant Poisson's ratio may violate the symmetry of the compliance matrix, potentially introducing mathematical inconsistencies in the constitutive formulation [52]. As shown in Section 3.4, when the growth-ring is taken into consideration, besides the v_{LT} shown in Table 2, v_{LR} also becomes the primary parameter that controls the magnitude of the transverse cupping deformation, which triggers the perpendicular to grain stress. As shown in [26], v_{RT} is a crucial parameter that affects stress concentration due to the growth-ring effect. Hence, further future experimental work on transverse hygro-mechanical behavior is needed to validate the accuracy of transverse stress predictions under moisture gradients.

4. Conclusion

This research conducted a 3D parametric multi-field FE analysis incorporating a time- and moisture-dependent constitutive model to provide a systematic evaluation of the residual stress that developed during the manufacturing process.

It is found that besides the longitudinal stress that is considered in the current design standard such as EC5 [12], there also exist non-negligible stresses in the transverse directions. The major causes of the longitudinal and transverse residual stresses can be attributed to three bending effects: the longitudinal bending ($M_Z^{St1,i}$) for curving each single board, the bending due to the spring-back effect ($-M_Z^{St3,N}$), and the bending (M_X) in the transverse direction caused by the Poisson effect. Moreover, due to the varying growth ring patterns in different board layers, the residual stress in radial and tangential directions can get intensified. The influence of the combination of these different stresses has not been discussed before, and it can cause the reduction of the load-carrying capacity of the beam.

In the current design standard, the magnitude of the longitudinal residual stress is considered to be influenced by the longitudinal stiffness, the board thickness, and the inner radius of the beam. In this study, it is revealed that the number of layers (n) can also cause up to a 12.5 % difference in the longitudinal residual stresses. Besides, the parameter $\frac{v_{LT} E_T}{E_L}$ (simplified as Poisson's ratio v_{LT} in some cases) is shown to significantly influence the magnitude of transverse residual stresses.

CRediT authorship contribution statement

Taoyi Yu: Writing – review & editing, Writing – original draft, Software, Methodology, Investigation, Conceptualization. **Ani Khaloian:** Writing – review & editing, Supervision, Methodology, Funding acquisition, Conceptualization. **Jan-Willem van de Kuilen:** Writing – original draft, Supervision, Funding acquisition, Conceptualization.

Declaration of competing interest

The authors declare that they have no known competing financial interests or personal relationships that could have appeared to influence the work reported in this paper.

Data availability

Data will be made available upon request.

References

[1] Blaß HJ, Sandhaas C. Timber Engineering - principles for design. KIT Scientific Publishing; 2017. https://doi.org/10.5445/KSP/1000069616

[2] Blaß HJ, Schmid M. Querzugfestigkeit von Vollholz und Brettschichtholz. Holz Roh Werkst 2001;58(6):456–66. https://doi.org/10.1007/s001070050460

[3] Dietsch P, Winter S. Structural failure in large-span timber structures: a comprehensive analysis of 230 cases. Struct Saf 2018;71:41–46. https://doi.org/10.1016/j.strusafe.2017.11.004

[4] Franke S, Franke B, Harte AM. Failure modes and reinforcement techniques for timber beams – state of the art. Const Buil Mater 2015;97:2–13. https://doi.org/10.1016/j.conbuildmat.2015.06.021

[5] Frese M, Blaß HJ. Statistics of damages to timber structures in Germany. Eng Struct 2011;33(11):2969–77. https://doi.org/10.1016/j.engstruct.2011.02.030

[6] Blass HJ, Eberhart O, Ehlbeck J, Gerold M. Wirkungsweise von eingeleimten Gewindestangen bei der Aufnahme von Querzugkräften in gekrümmten Biegeträgern und Entwicklung von Bemessungsgrundlagen. Teil 3; 1996. Karlsruhe 1996. (Forschungsbericht der Versuchsanstalt für Stahl, Holz und Steine, Abt. Ingenieurholzbau, Universität Karlsruhe.). https://publikationen.bibliothek.kit.edu/100196.

[7] Jönsson J. Load carrying capacity of curved glulam beams reinforced with self-tapping screws. Holz Roh Werkst 2005;63(5):342–46. https://doi.org/10.1007/s00107-005-0016-5

[8] Fueyo JG, Cabezas JA, Rubio MP, Domínguez M. Reduction of perpendicular-to-grain stresses in the apex zone of curved beams using glued-in rods. Mater Struct 2010;43(4):463–74. https://doi.org/10.1617/s11527-009-9503-1

[9] Rug W. 100 Jahre Hetzer–Patent. Bautechnik 2006;83(8):533–40. https://doi.org/10.1002/bate.200610046

[10] Chai H, Guo Z, Yuan PF. Developing a mold-free approach for complex glulam production with the assist of computer vision technologies. Autom Constr 2021;127:103710. https://doi.org/10.1016/j.autcon.2021.103710

[11] Zhang H, Shen M, Deng Y, Andras P, Sukontasukkul P, Yuen TYP, et al. A new concept of bio-based prestress technology with experimental proof-of-concept on bamboo-timber composite beams. Const Buil Mater 2023;402:132991. https://doi.org/10.1016/j.conbuildmat.2023.132991

[12] DIN EN 1995-1-1. Eurocode 5: design of timber structures – Part 1-1: General-common rules and rules for buildings.

[13] Aondio P, Winter S, Kreuzinger H. Calculation of cylindrical shells from wood or wood based products and consideration of the stress relaxation. In: Görlacher R, editor. International Network on Timber Engineering Research; Bath, United Kingdom. 2014. pp. 47–12–1.

[14] Aicher S, Dill-Langer G, Ranta-Maunus A. Duration of load effect in tension perpendicular to the grain of glulam in different climates. Eur J Wood Wood Prod 1998;56(5):295–305. https://doi.org/10.1007/s001070050323

[15] Dietsch P, Gamper A, Merk M, Winter S. Monitoring building climate and timber moisture gradient in large-span timber structures. J Civ Struct Health Monit 2015;5(2):153–65. https://doi.org/10.1007/s13349-014-0083-6

[16] Maas JM, Grönquist P, Furrer J, Studer V, Malvetti A, Rüggeberg M, et al. Residual stresses in adhesively bonded wood determined by a bilayer flexion reporter system. Wood Sci Technol 2022;56(5):1293–313. https://doi.org/10.1007/s00226-022-01402-0

[17] Forest Products Laboratory. Wood handbook—wood as an engineering material: General technical report FPL-GTR-190, Madison. 2010.

[18] van der Velden A, Kuipers J. Directives for the fabrication of load-bearing structures of glued timber. In: CIB-W18 meeting; 1976.

[19] Aicher S, Dill-Langer G. Effect of lamination anisotropy and lay-up in glued-laminated timbers. J Struct Eng 2005;131(7):1095–103. https://doi.org/10.1061/(ASCE)0733-9445(2005)131:7(1095)

[20] Franke B, Franke S, Müller A, Schiere M. Long-term behaviour of moisture content in timber constructions–relation to service classes. In: International Network on Timber Engineering Research Meeting 49; vol. 5. 2016. p. 19–23.

[21] Lee SS, Pan SJ, Jeong GY. Effects of size, species and adjacent lamina on moisture related strain in glulam. Wood Fiber Sci 2019;51(2):101–18. https://doi.org/10.22382/wfs-2019-013

[22] Fink G. Influence of varying material properties on the load-bearing capacity of glued laminated timber [Ph.D. thesis]. ETH Zurich; 2014. https://doi.org/10.3929/ETHZ-A-010108864

[23] Kandler G, Füssl J. A probabilistic approach for the linear behaviour of glued laminated timber. Eng Struct 2017;148:673–85. https://doi.org/10.1016/j.engstruct.2017.07.017

[24] Bezabeh MA, Bitsuamlak GT, Popovski M, Tesfamariam S. Probabilistic serviceability-performance assessment of tall mass-timber buildings subjected to stochastic wind loads: part I - structural design and wind tunnel testing. J Wind Eng Ind Aerod 2018;181:85–103. https://doi.org/10.1016/j.jweia.2018.08.012

[25] Kukk V, Kers J, Kalamees T, Wang L, Ge H. Impact of built-in moisture on the design of hygrothermally safe cross-laminated timber external walls: a stochastic approach. Build Environ 2022;226:109736. https://doi.org/10.1016/j.buildenv.2022.109736. https://www.sciencedirect.com/science/article/pii/S0360132322009660

[26] Yu T, Khaloian-Sarnaghi A, Seeber F, van de Kuilen J-W. Stochastic fe analysis of stress concentrations in curved glulam beams due to the uncertainty of material direction. Const Buil Mater 2023;393:131537. https://doi.org/10.1016/j.conbuildmat.2023.131537

[27] Yu T, Seeber F, Khaloian A, van de Kuilen J-W. Growth-ring effect on moisture-induced stress and damage development in glued laminated timber. Wood Sci Technol 2025;59(4). https://doi.org/10.1007/s00226-025-01647-5

[28] Yu T, Khaloian A, van de Kuilen J-W. An improved model for the time-dependent material response of wood under mechanical loading and varying humidity conditions. Eng Struct 2022;259:114116. https://doi.org/10.1016/j.engstruct.2022.114116

[29] Hunt DG. Linearity and non-linearity in mechano-sorptive creep of softwood in compression and bending. Wood Sci Technol 1989;23(4):323–33. https://doi.org/10.1007/BF00353248

[30] Hassani MM, Wittel FK, Hering S, Herrmann HJ. Rheological model for wood. Comput Methods Appl Mech Eng 2015;283:1032–60. https://doi.org/10.1016/j.cma.2014.10.031

[31] O'Ceallaigh C, Sikora K, McPolin D, Harte AM. Modelling the hygro-mechanical creep behaviour of FRP reinforced timber elements. Const Buil Mater 2020;259:119899. https://doi.org/10.1016/j.conbuildmat.2020.119899

[32] Massaro FM, Malo KA. Long-term behaviour of Norway spruce glulam loaded perpendicular to grain. Eur J Wood Wood Prod 2019;77(5):821–32. https://doi.org/10.1007/s00107-019-01437-4

[33] Avramidis S. Evaluation of three-variable models for the prediction of equilibrium moisture content in wood. Wood Sci Technol 1989;23(3):251–57. https://doi.org/10.1007/BF00367738

[34] Deutscher Wetterdienst. Klimadaten des climate data centers (CDC) des Deutschen Wetterdienstes [8/25/2024]. https://www.dwd.de/DE/leistungen/cdc/cdc_ueberblick-klimadaten.html

[35] Hering S, Niemz P. Moisture-dependent, viscoelastic creep of European beech wood in longitudinal direction. Holz Roh Werkst 2012;70(5):667–70. https://doi.org/10.1007/s00107-012-0600-4

[36] Hering S. Charakterisierung und modellierung der materialeigenschaften von rotbuchenholz zur simulation von holzverklebungen [Ph.D. thesis]. ETH Zurich; 2011. https://www.research-collection.ethz.ch/bitstream/handle/20.500.11850/46378/1/eth-5340-01.pdf

[37] Olek W, Perré P, Weres J. Inverse analysis of the transient bound water diffusion in wood. Holzforschung 2005;59(1):38–45. https://doi.org/10.1515/HF.2005.007

[38] Golovin KS. One problem in statics of an elastic body (in Russian). Izvestia St Peterburg Prakt Tekhnol Inst 1881;3:373–410.

[39] Timoshenko SP, Goodier JN. Theory of elasticity. 2nd Edition. New York: McGraw-Hill Book Company; 1951. [Engineering societies monographs].

[40] Möhler K, Blumer H. Gekruemmte Brettschichttraeger mit konstanter Querschnittschoehe oder mit geneigtem Obergurt. Universität Karlsruhe (TH); 1978.

[41] Ehlbeck J, Kürth J. Tapered, curved and piched cambered beams. In: Structural timber education program (STEP) B8; 1995. p. 1–8. https://img1.wsimg.com/blobby/go/54d4f5b7-7f4f-4cf8-a53b-1fefa7dbd9a1/downloads/STEP%20B8.pdf?ver=1749719933565.

[42] Schmidt J, Kaliske M. Models for numerical failure analysis of wooden structures. Eng Struct 2009;31(2):571–79. https://doi.org/10.1016/j.engstruct.2008.11.001. https://www.sciencedirect.com/science/article/pii/S0141029608003623

[43] Sandhaas C. Mechanical behviour of timber joints with slotted-in steel plates [Doctoral dissertation]. Zutphen: Delft University of Technology; 2012.

[44] de Santis Y, Aloisio A, Pasca DP, Fragiacomo M, Dombrowski F. Evaluation of the shear size effect in glued laminated timber using a stochastic fe model calibrated on 17000 glue-line tests. Const Buil Mater 2023;399:132488. https://doi.org/10.1016/j.conbuildmat.2023.132488

[45] Jenkel C, Leichsenring F, Graf W, Kaliske M. Stochastic modelling of uncertainty in timber engineering. Eng Struct 2015;99:296–310. https://doi.org/10.1016/j.engstruct.2015.04.049

[46] Kandler G, Lukacevic M, Zechmeister C, Wolff S, Füssl J. Stochastic engineering framework for timber structural elements and its application to glued laminated timber beams. Const Buil Mater 2018;190:573–92. https://doi.org/10.1016/j.conbuildmat.2018.09.129

[47] Steiger R. Interaction of shear stress and stresses perpendicular to the grain. In: CIB-W18 meeting; 2011.

[48] van de Kuilen J-W, Grad W, Ravenshorst G, Antonelli V, Kovryga A. Shear strength values for soft- and hardwoods: 50-06-1. In: International Network on Timber Engineering Research Meeting 50; 2017.

[49] Huč S, Svensson S. Coupled two-dimensional modeling of viscoelastic creep of wood. Wood Sci Technol 2018;52(1):29–43. https://doi.org/10.1007/s00226-017-0944-3

[50] Jiang J, Erik Valentine B, Lu J, Niemz P. Time dependence of the orthotropic compression Young's moduli and Poisson's ratios of Chinese fir wood. Holzforschung 2016;70(11):1093–101. https://doi.org/10.1515/hf-2016-0001

[51] Kawahara K, Ando K, Taniguchi Y. Time dependence of Poisson's effect in wood IV: influence of grain angle. J Wood Sci 2015;61(4):372–83. https://doi.org/10.1007/s10086-015-1477-8

[52] Huč S, Svensson S. Influence of grain direction on the time-dependent behavior of wood analyzed by a 3d rheological model. A mathematical consideration. Holzforschung 2018;72(10):889–97. https://doi.org/10.1515/hf-2017-0180